Ultrafast Electron and Hole Relaxation Pathways in Few-Layer MoS2

Nie, Zhaogang; Long, Run; Teguh, Jefri S.; Huang, Chung-Che; Hewak, Daniel W.; Yeow, Edwin K. L.; Shen, Zexiang; Prezhdo, Oleg V.; Loh, Zhi-Heng

2015

https://hdl.handle.net/10356/79259

https://doi.org/10.1021/acs.jpcc.5b05048

Ultrafast Electron and Hole Relaxation Pathways in Few-Layer MoS$_2$

Zhaogang Nie,[a] Run Long,[b,c,d] Jefri S. Teguh,[a] Chung-Che Huang,[e] Daniel W. Hewak,[e] Edwin K. L. Yeow,[a] Zexiang Shen,[f,g,h] Oleg V. Prezhdo,[b] and Zhi-Heng Loh[a,f*]*

[a] Division of Chemistry and Biological Chemistry, School of Physical and Mathematical Sciences, Nanyang Technological University, Singapore 637371, Singapore

[b] Department of Chemistry, University of Southern California, Los Angeles, California 90089, United States

[c] School of Physics, Complex Adaptive Systems Laboratory, University College Dublin, Belfield, Dublin 4, Ireland

[d] College of Chemistry, Key Laboratory of Theoretical & Computational Photochemistry of Ministry of Education, Beijing Normal University, Beijing, 100875, P. R. China.

[e] Optoelectronics Research Centre, University of Southampton, Southampton SO17 1BJ, United Kingdom

[f] Division of Physics and Applied Physics, School of Physical and Mathematical Sciences, Nanyang Technological University, Singapore 637371, Singapore

[g] Centre for Disruptive Photonic Technologies, School of Physical and Mathematical Sciences, Nanyang Technological University, Singapore 637371, Singapore

[h] Division of Materials Technology, School of Materials Science and Engineering, Nanyang Technological University, Singapore 639798, Singapore

---

* Corresponding Authors: (O.V.P.) E-mail: prezhdo@usc.edu. Telephone: +1 (213) 821-3116.

(Z.-H.L.) E-mail: zhiheng@ntu.edu.sg. Telephone: +65 6592-1655.

Abstract

Femtosecond optical pump-probe spectroscopy is employed to elucidate the band-selective ultrafast carrier dynamics of few-layer MoS_2. Following narrowband resonant photoexcitation of the exciton A transition, the sub-picosecond to picosecond relaxation dynamics of the electron and the hole at the K valley are separately interrogated by a broadband probe pulse. The temporal evolution of the spectral first moment reveals nonexponential intravalley relaxation dynamics in the conduction band. Fluence dependence measurements suggest that this relaxation process is predominantly mediated by acoustic phonon emission. Intervalley scattering of carriers from the K valley to the extrema of the conduction and valence bands is also observed *via* the decay of the spectral zeroth moment. In addition, second-order Raman scattering leads to the emergence of sidebands in the normalized differential transmission spectra. The observed two-phonon energies and the fluence-dependent time constants suggest that the E_{1g} LO phonon and the LA phonon participate in intervalley scattering in the conduction and valence bands, respectively. *Ab initio* nonadiabatic molecular dynamics simulations yield time constants of 0.80 ps and 0.72 ps for intra- and intervalley electronic relaxation, respectively; the latter agrees well with experiment. Finally, the normalized differential transmission spectra reveal a two-electron shake-up satellite that originates from band-edge radiative recombination and the simultaneous excitation of a hole from K_{v1} to K_{v2}. From its spectral position, a K_{v1}–K_{v2} spin-orbit splitting of 1166 ± 1 cm^{-1} is deduced. The observation of the two-electron transition points to the existence of strong electron correlation in photoexcited few-layer MoS_2.

Keywords: MoS_2, ultrafast carrier dynamics, carrier-phonon scattering, second-order Raman scattering, two-electron transition

Introduction

Few-layer two-dimensional transition metal dichalcogenides have recently emerged as promising candidates for atomically thin semiconducting electronic materials,[1,2] with molybdenum disulfide (MoS_2) being the most commonly studied to date.[3] Good electron mobilities of ~200 cm^{2}Vs^{-1} and on/off ratios exceeding 10^8, for example, have been demonstrated in field-effect transistors based on monolayer MoS_2.[4] In addition, the existence of a direct band gap transition in the monolayer regime[5,6] along with the chemical tunability of the associated band-edge photoluminescence from the visible to the near-infrared[7,8] make these materials well-suited to a variety of optoelectronic applications.[9] Moreover, in the case of monolayer TMDs, there exists two inequivalent but energetically degenerate valleys at the corners of the first Brillouin zone, labeled K and K', as well as opposite spin projections for the two spin-orbit-split valence bands at the K and K' valleys;[10–13] the energy gap between the spin-orbit-split valence bands have been measured by steady-state optical spectroscopy.[5] The above implies coupled spin and valley degrees of freedom which are addressable by circularly polarized light, thus heralding the potential application of monolayer TMDs to spintronics and valleytronics.[10,14]

In the specific realm of carrier transport and electrical switching, earlier studies suggest that field-effect transistors (FET) based on multilayer MoS_2 exhibit superior performance characteristics compared to those that employ single-layer MoS_2. The carrier mobility has been shown to increase with the number of layers in a non-monotonic fashion, with a record-high mobility of 700 cm^{2}V^{-1}s^{-1} achieved for a FET that comprises 10-nm-thick MoS_2 overcoated by an Al_2O_3 dielectric layer.[15] The enhanced mobility supports higher on-state currents, which in turn enables larger operation bandwidths.[16] Moreover, single-layer devices have been shown to suffer from high ~GΩ resistance, possibly due to the large Schottky barrier between the electrode

and the TMD monolayer.[17] The higher electrical noise associated with monolayer devices[18] further limits their application to sensing,[19] for example. Finally, phototransistors that employ multilayer MoS_2 have one- to two-orders of magnitude higher photoresponse at visible wavelengths[20] than their single-layer counterparts.[21] As a result of its indirect band gap, multilayer MoS_2 also allow the responsivies of phototransistors to extend to the near-infrared.[20,22] Taken together, these studies suggest that additional investigations of the electronic properties of multilayer MoS_2 are desired to further increase its technological relevance.

The electronic and optoelectronic characteristics of semiconductors are, to a large extent, governed by their fundamental carrier dynamics.[23] For example, carrier-carrier and carrier-phonon scattering processes are known to limit carrier mobilities. In high-field transport, these scattering processes also participate in the cooling of carriers that are heated by the presence of large external electric fields. For valleytronic materials, possible loss of valley polarization due to carrier-carrier and carrier-phonon scattering must be taken into account. The above considerations have motivated recent studies of the ultrafast carrier dynamics of single-layer and few-layer TMDs. Results from optical pump-probe spectroscopy on MoS_2 performed with circularly polarized pulses suggest the preservation of valley polarization on a few-picosecond timescale,[24,25] in agreement with results obtained from time-resolved photoluminescence measurements.[26,27] Sub-picosecond dynamics that are associated with the coherent coupling of electrons in different valleys,[25] exciton-exciton scattering,[28] carrier thermalization and cooling[29] have also been observed by optical pump-probe spectroscopy, in addition to rapid exciton-exciton annihilation[30] in MoS_2 and ultrafast charge transfer in MoS_2/WS_2 van der Waals heterostructures.[31] By augmenting a spatial dimension to optical pump-probe studies, optical pump-probe microscopy have yielded exciton lifetimes and diffusion coefficients for a variety of

TMDs.[32] Spatially-resolved ultrafast exciton trapping and carrier-phonon scattering dynamics of single-layer to bulk MoS_2 have been observed as well.[33] The above optical measurements are complemented by optical-pump terahertz-probe measurements, which reveal photoconductivity responses of monolayer MoS_2 that can be explained by trion formation followed by their decay over tens of picoseconds *via* nonradiative recombination at defect sites.[34] On sub-picosecond timescales, the decay of terahertz photoconductivity is assigned to defect-mediated carrier recombination.[35]

The aforementioned time-resolved optical pump-probe studies of TMDs have yielded information on the combined dynamics of the electrons and the holes. This is because pump-probe spectroscopy is inherently sensitive to absorption saturation induced by phase-space filling, such that the normalized differential transmission signal $\Delta T/T \propto f_e + f_h$ is proportional to the sum of the electron (f_e) and the hole (f_h) distribution functions.[36] It remains desirable, however, to discern the separate time-evolution of the electrons and the holes. Beyond their fundamental interest, the individual ultrafast dynamics of the electron and the hole also provide the conceptual framework for understanding the electron and hole transport properties of TMD-based electronic devices.

Here, we report the use of optical pump-probe spectroscopy to elucidate the separate ultrafast relaxation dynamics of electrons and holes of a five-layer MoS_2 sample. Our experimental approach (Figure 1a) is inspired by earlier optical pump-probe studies of GaAs, in which photoexcitation of the heavy- and light-hole valence bands was followed by probing the interband transition from the higher-energy spin-orbit split-off valence band $\Gamma_{v,so}$.[37,38] As the low-energy pump excitation does not create holes at $\Gamma_{v,so}$, the probe pulse interrogates only the

electronic dynamics in the conduction band Γ_c. In the present work, narrowband resonant excitation of the A exciton transition by the pump pulse (Figure 1b) promotes electrons from K_{v1} to K_c, following which the differential transmission of a broadband probe pulse that spans the A and B exciton transitions is collected as a function of pump-probe time delay. The B exciton probe transition, which promotes electrons from the spin-orbit split-off K_{v2} band to K_c, is insensitive to the time-dependent hole distribution function at K_{v1} that is created by the pump pulse. Therefore its temporal evolution only reflects the electron dynamics at K_c. With knowledge of the electron dynamics, the hole dynamics can then be recovered from the temporal evolution of the A exciton probe transition, which bears contributions from both electron and hole dynamics. This approach contrasts with the non-selective, broadband excitation by 10-fs pulses that was employed in our previous work, which creates an energetically broad carrier distribution and therefore obfuscates the separation of electron and hole dynamics.[29]

It is important to note that the pump fluences employed in this work yield two-dimensional carrier densities that span $(0.5 - 2.4) \times 10^{13}$ cm^{-2}, which is comparable to the Mott density of MoS$_2$ ($\sim 10^{13}$ cm^{-2}).[39] As such, the ultrafast dynamics that are reported herein are those of free carriers in an electron-hole plasma rather than excitons. Since the optical band gap of trilayer MoS$_2$ (1.35 eV)[22] already approaches the indirect band gap of the bulk (1.29 eV),[40] and that the band structure of few-layer MoS2 is relatively independent of layer number,[41] we believe that the present results obtained on five-layer MoS$_2$ are pertinent to the understanding of carrier transport phenomena in multilayer MoS$_2$-based electronic devices. Our measurements reveal timescales for electron and hole relaxation *via* intervalley and intravalley carrier-phonon scattering. More importantly, the fluence-dependence of the relaxation dynamics and the appearance of previously unobserved second-order Raman sidebands in the $\Delta T/T$ spectra allow

the first experimental identification of characteristic phonon energies and phonon modes that dominate carrier-phonon scattering. Therefore, the present investigation elucidates, beyond the carrier cooling timescales, the pathways for carrier relaxation in few-layer MoS_2 with unprecedented detail. Finally, a peak that is redshifted from the exciton A peak by the spin-orbit splitting is observed in the $\Delta T/T$ spectra. This peak is attributed to a two-electron optical transition whose appearance suggests the existence of strong electron correlation in the photoexcited few-layer MoS_2 system.

Results and Discussion

Following optical excitation of the exciton A transition in five-layer MoS_2, the carriers undergo ultrafast thermalization on the <20-fs timescale before the onset of carrier cooling.[29] Carrier cooling can occur *via* intravalley relaxation and intervalley scattering of carriers to other valleys (Figure 2).[42] Both processes are mediated by phonon emission to fulfill energy and momentum conservation requirements. In the case of few-layer MoS_2, the extrema of the valence and conduction bands are located at the Γ and Q valleys, respectively,[43,44] thereby making the intervalley $K_v \rightarrow \Gamma_v$ and $K_c \rightarrow Q_c$ scattering processes energetically accessible for holes and electrons, respectively. Because intravalley scattering is accompanied by a time-dependent change in the energy gap of the K valley (Figure 2), it can be discerned from the temporal evolution of the spectral first moment, defined as

$$\langle \lambda^{(1)}(t) \rangle = \frac{\int_{\lambda_i}^{\lambda_f} d\lambda \; \lambda \; \Delta T(\lambda, t)/T(\lambda)}{\int_{\lambda_i}^{\lambda_f} d\lambda \; \Delta T(\lambda, t)/T(\lambda)}, \tag{1}$$

where t is the pump-probe time delay, and λ_i and λ_f correspond to the limits of the integral. On the other hand, timescales for the intervalley scattering of carriers away from the K valley are obtained by analyzing the decay of the spectral zeroth moment, given as

$$\langle \lambda^{(0)}(t) \rangle = \frac{\int_{\lambda_i}^{\lambda_f} d\lambda \; \Delta T(\lambda, t)/T(\lambda)}{\lambda_f - \lambda_i}.$$ (2)

Intuitively, $\langle \lambda^{(1)} \rangle$ is related to the energy gap between the bands which are optically coupled by the probe pulse, whereas $\langle \lambda^{(0)} \rangle$ yields the carrier populations at the initially excited Franck-Condon region.[45] Note that by virtue of its long timescale ($\gtrsim 100$ ps),[33] carrier recombination in few-layer MoS_2 is not expected to contribute significantly to the picosecond decay of $\langle \lambda^{(0)}(t) \rangle$ observed in this work.

The normalized differential transmission spectra $\Delta T/T$ collected at 300 K as a function of pump-probe time delay for excitation pump fluences of 0.06, 0.14, and 0.29 mJ/cm^2 are shown in Figures 3a, 3b, and 3c, respectively. At low pump fluence, the $\Delta T/T$ spectra reveal positive $\Delta T/T$ features that are ascribed to ground state bleaching of the exciton A and B transitions and stimulated emission at the exciton A transition. A negative $\Delta T/T$ feature that is especially prominent on the low-energy side of the probe spectrum is also observed and is assigned to excited state absorption involving intersubband transitions.[25,28,29] Employing higher pump fluences results in the emergence of positive $\Delta T/T$ sidebands on the low-energy side of the exciton A and B probe transitions (Figure 3c).

The time-evolution of $\langle \lambda^{(1)}(t) \rangle$ in the spectral region of the exciton B probe yields the intravalley electronic relaxation dynamics at K_c. The computed $\langle \lambda^{(1)}(t) \rangle$ traces for excitation

pump fluences of 0.06, 0.14, and 0.29 mJ/cm^2 are shown in Figure 4. The observed blueshift

with increasing time delay is due to the dynamic Burstein-Moss effect that accompanies

intravalley carrier relaxation.[46,47] The nonexponential behavior of the spectral blueshift points to

electron cooling dynamics that cannot adequately be described in terms of a single rate constant,

as prescribed by the Fermi Golden Rule. On the other hand, the excellent fit of the spectral

blueshift to the Gaussian decay profile (see Supplementary Information Table 1 for the fit

parameters) suggests the need for a quantum dynamical description of electron cooling in few-

layer MoS$_2$.[48,49] The Gaussian decay time constant $\tau_e^{(1)}$, equivalent to the standard deviation of a

Gaussian function, decreases from 1.77 ± 0.08 ps at a pump fluence of 0.06 mJ/cm^2 to $1.34 \pm$

0.02 ps for both 0.14 and 0.29 mJ/cm^2 pump fluences.

Ab initio studies of monolayer MoS$_2$ show that intravalley relaxation at K$_c$ is primarily

mediated by the emission of the A$_{1g}$ longitudinal optical (LO) phonon.[50,51] The cooling power of

LO phonons is also predicted to be two orders of magnitude larger than acoustic phonons,[52]

thereby favoring LO phonon emission as the more efficient carrier relaxation pathway. In light of

these theoretical findings, LO phonon emission might be expected to be the major contributor to

the intravalley electronic relaxation observed here. The fluence dependence exhibited by $\tau_e^{(1)}$,

however, is incompatible with the participation of LO phonons in intravalley relaxation. This is

because carrier cooling *via* LO phonon emission is highly susceptible to the hot phonon

effect,[53,54] which leads to a drastic reduction in cooling power at higher carrier densities due to

the buildup of a large, nonequilibrium LO phonon population. On the other hand, the following

considerations point to acoustic phonon emission as the dominant route to electronic cooling in

the present work. First, the observed fluence dependence of $\tau_e^{(1)}$ can be explained by the increase

in cooling power of acoustic phonons with carrier density.[52] Moreover, the acoustic phonons can

be assumed to be in thermal equilibrium with the lattice and the substrate, thus rendering them relatively insensitive to the hot phonon effect. Second, the excess electronic energy of $E_e \sim 620 \pm 230$ cm^{-1} (see Supporting Information Figure S1) is comparable to the LO phonon frequency of $\omega_{LO} \sim 400$ cm^{-1} under our experimental conditions. Because the dissipation of excess energies below $\hbar\omega_{LO}$ cannot proceed *via* the emission of LO phonons, acoustic phonon emission is expected to account for a sizeable fraction of the electronic energy loss.

Besides intravalley carrier relaxation, carriers that are initially generated at the K valley can also relax to other valleys *via* intervalley scattering. In few-layer MoS$_2$, the K$_c \rightarrow$ Q$_c$ and K$_v \rightarrow \Gamma_v$ scattering pathways are available for the electrons and holes, respectively. The spectral zeroth moment time traces $\langle \lambda^{(0)}(t) \rangle$ computed about the exciton B transition are shown in Figure 5a for pump fluences of 0.06, 0.14, and 0.29 mJ/cm^2. The decrease in $\langle \lambda_B^{(0)}(t) \rangle$ on the picosecond timescale is a result of intervalley scattering of electrons from the K valley of the conduction band. On the other hand, the temporal evolution of the hole population at the K valley is reflected in the difference signal $\langle \lambda_{A-B}^{(0)}(t) \rangle = \langle \lambda_A^{(0)}(t) \rangle - \langle \lambda_B^{(0)}(t) \rangle$ (Figure 5b). Both $\langle \lambda_B^{(0)}(t) \rangle$ and $\langle \lambda_{A-B}^{(0)}(t) \rangle$ traces can be fit to exponential decays to give time constants $\tau_e^{(0)}$ and $\tau_h^{(0)}$, respectively (Table 1). The exponential decay dynamics of intervalley scattering is consistent with the indirect band gap nature of few-layer MoS$_2$, which presents a high density of states into which the carriers at the K valley can scatter, hence ensuring the validity of the Fermi Golden Rule. Furthermore, $\tau_e^{(0)}$ and $\tau_h^{(0)}$ are found to exhibit opposite trends in their pump fluence dependence: $\tau_e^{(0)}$ increases with excitation pump fluence whereas $\tau_h^{(0)}$ decreases. Employing the same considerations that account for the observed fluence dependence of the intravalley electronic relaxation timescales (see above),[52] we can tentatively infer that intervalley

scattering in the conduction band is primarily mediated by LO phonons, whereas intervalley scattering in the valence band involves the participation of acoustic phonons.

The sidebands in the $\Delta T/T$ spectra that emerge under high-excitation fluence conditions (Figure 3c) provide further evidence for the participation of LO and acoustic phonons in the intervalley scattering processes in the conduction and valence bands, respectively. The sidebands develop on the low-energy side of the exciton A and B transitions and evolve concomitantly with the primary peaks. The latter observation suggests that the sidebands are not a product of carrier cooling. Here, the origin of these sidebands is assigned to second-order Raman scattering (Figure 6a).[55,56] Starting from the initial electron and hole distributions generated by the pump pulse, the successive emission of two phonons of opposite momenta $-\hbar q$ and $+\hbar q$ leads to the reappearance of carriers in the original K valley. By the conservation of energy, these carriers are lower in energy than the initial distributions by $2\hbar\omega_q$. The subset of lower-energy carriers gives rise to additional ground-state bleaching and stimulated emission transitions which result in the sidebands in the $\Delta T/T$ spectra. The characteristic energy of the two-phonon transition is consequently given by the energetic separation between the primary exciton peak and its sideband, whose positions can be delineated from the second-derivative $\Delta T/T$ spectra (Figure 6b). At a time delay of 200 fs, the second-derivative spectrum shows an energy separation of $\Delta E_B = 550 \pm 13$ cm^{-1} between the exciton B transition and its sideband, whereas that for the exciton A transition and its sideband is $\Delta E_A = 462 \pm 13$ cm^{-1} (Figure 6c, also see Supporting Information Figure S2). These two-phonon energies are in good agreement with the $2E_{1g}(\Gamma)$ and $2LA(M)$ two-phonon peaks that appear in the spontaneous resonant Raman spectrum at 565 and 450 cm^{-1}, respectively (see Supporting Information Figure S3).[55,57,58] Our result therefore

indicates that the two-phonon carrier-phonon scattering processes in the conduction and valence bands are mediated by the E_{1g} LO phonon and the LA phonon, respectively.

From the above analysis, we infer that two-phonon carrier-phonon scattering processes in the conduction and valence bands involve the E_{1g} LO phonon and the LA phonon, respectively. For an initial population of carriers at the K valley with excess energies of $E_e \sim 620 \pm 230$ cm^{-1} and $E_h \sim 820 \pm 290$ cm^{-1}, respectively, the energetically accessible two-phonon scattering pathways are $K_c \rightarrow Q_c \rightarrow K_c$ for the conduction band and $K_v \rightarrow \Gamma_v \rightarrow K_v$ for the valence band.[43,44] It is conceivable that the same phonons are primarily responsible for the net depopulation of carriers from the K valley *via* one-phonon $K_c \rightarrow Q_c$ and $K_v \rightarrow \Gamma_v$ intervalley scattering. That is, the intervalley scattering that leads to the observed decay in the $\langle \lambda_B^{(0)}(t) \rangle$ and $\langle \lambda_{A-B}^{(0)}(t) \rangle$ time traces are mediated by the E_{1g} LO and LA phonons, respectively. Because the cooling power of optical phonons decreases with carrier density whereas that of acoustic phonons increases, $\tau_e^{(0)}$ is found to increase with carrier density, opposite to the fluence dependence observed for $\tau_h^{(0)}$. Furthermore the presence of second-order Raman sidebands even at early time delays ($t < 200$ fs) implies the onset of intervalley scattering immediately upon photoexcitation, which in turn raises the possibility that the same phonon modes might be responsible for the previously observed sub-20-fs intervalley scattering dynamics in few-layer MoS$_2$.[29]

Ab initio nonadiabatic molecular dynamics simulations are performed to elucidate the various electronic relaxation channels that are available in photoexcited few-layer MoS$_2$. Starting from a population of electrons in the K_c valley with an initial excess energy of 1000 cm^{-1}, relaxation *via* intervalley scattering is found to occur with time constants of 75 fs and 0.72 ps

(Figure 7a). The latter is in good agreement with the present experimental results, while the fast component is consistent with the timescale for carrier thermalization in few-layer MoS_2.[29] The simulation also agrees with the experiment in showing that the intravalley electron-phonon scattering requires longer time than the intervalley scattering. However, the simulated time trace for the intravalley relaxation of the conduction band electrons is different from those obtained from experiment. The simulated time trace is well represented by an exponential decay with a time constant of 0.80 ps (Figure 7a) whereas the experimental data strongly suggests nonexponential dynamics (Figure 4). Moreover, experiments show that the time required for the hot electron population to reach $1/e$ of its initial energy is 1.9 ps, approximately a factor of two longer than the simulated time. These discrepancies can be attributed to the excess energy being higher in the simulations (1000 cm^{-1}) than in the experiments (620 cm^{-1}), as indicated by sample calculations. The additional phonon-mediated relaxation pathways that arise from the higher excess energy effectively enhance energy dissipation and suppress nonexponential relaxation behavior.

It is interesting to note that the simulated intravalley and intervalley relaxation time traces reveal the existence of weak oscillatory features. The FFT power spectra (Figure 7b) yield the frequencies of phonons which participate in the electronic cooling process. Both power spectra exhibit a low-frequency band (<100 cm^{-1}), as well as a high-frequency peak at 800 cm^{-1}. The latter is consistent with the first overtone frequency of the A_{1g} LO phonon; its fundamental frequency at 400 cm^{-1} is apparent in the FFT power spectrum of the intervalley relaxation trajectory. The low-frequency band likely arises from acoustic phonons, although contributions from interlayer shearing modes are also possible.[59] These simulation results should be compared with the experimental results, which suggest that intravalley and intervalley electronic relaxation

are dominated by the emission of acoustic phonons and the E_{1g} LO phonon, respectively. It is likely that the larger excess energies employed in the simulations than in the experiments enhance the contributions of the higher frequency LO phonons to the electronic cooling.

Finally, we note that the second-derivative $\Delta T/T$ spectra reveal an electronic transition at 729 nm that is Stokes shifted by $\Delta E_{A'} \sim 1200$ cm^{-1} from the exciton A transition (see arrow in Figure 6b). This feature becomes more prominent with increasing time delay (Figure 8a) and is apparent even with the lowest excitation fluence (0.06 mJ/cm^2) employed in our experiments. The absence of spectral features at such high frequencies in the room-temperature Raman spectrum of MoS_2 excludes the possibility of associating $\Delta E_{A'}$ with a multiphonon Raman scattering process.[60] We instead consider an electronic origin for $\Delta E_{A'}$ due to its similarity to the 0.15-eV spin-orbit splitting of the valence band at the K valley.[5,6] Here, the electronic transition at 729 nm is tentatively assigned to a radiative shake-up satellite, in accord with its appearance on the low-energy side of the exciton A transition. Its existence as a peak atop the negative-going signal in the $\Delta T/T$ spectra is consistent with the stimulated emission nature of the transition. Based on the Q_c–K_c and Γ_v–K_{v1} energy differences of 3500 and 4600 cm^{-1}, respectively, stimulated emission of the phonon-assisted $Q_c \rightarrow K_{v1}$, $K_c \rightarrow \Gamma_v$, and $Q_c \rightarrow \Gamma_v$ indirect transitions can be ruled out as a possible explanation for the observed feature at 729 nm, for which the Stokes shift relative to the exciton A transition is only ~ 1200 cm^{-1}.

In the radiative shake-up process, originally uncovered in Auger transitions in the X-ray,[61] the radiative recombination of carriers accompanies the simultaneous excitation of the system. The conservation of energy requires the energy of the emitted photon to be downshifted from the band gap by the quantum of excitation. Shake-up satellites have previously been

observed in the photoluminescence spectra of CdZnSe/ZnSe core-shell nanocrystals[62] and doped semiconductors.[63,64] In the latter, the radiative recombination of excitons or free carriers is accompanied by the excitation of the dopant atoms. For the CdZnSe/ZnSe nanocrystals, radiative recombination of positive trions occurs concomitantly with the excitation of the remaining hole into higher-energy valence states. In the case of MoS_2, we postulate that the excitation of holes from K_{v1} to K_{v2} accompanies the probe pulse-stimulated radiative recombination of carriers at the band edge (Figure 8b). Because part of the energy released by band-edge radiative recombination E_r is used to excite the hole from K_{v1} to the spin-orbit-excited K_{v2} band, the final energy of the emitted photon is $h\nu = E_r - \Delta E_{so}$, where ΔE_{so} is the energy gap between K_{v1} to K_{v2}. Such a two-electron transition, in which a single photon drives the excitation and/or de-excitation of two electrons, is a hallmark of strong electron correlation.[65] While the observation of two-electron transitions in layered two-dimensional materials is unprecedented, their appearance in the present work is perhaps unsurprising in view of the few-nanometer spacing between adjacent carriers (corresponding to two-dimensional carrier densities of ~10^{13} cm^{-2}). The proximity between carriers leads to strong carrier-carrier interactions from which the two-electron transitions emerge. Interestingly, the energetic separation $\Delta E_{A'}$ is found to be time-dependent, starting from an initial value of 1218 ± 10 cm^{-1} and asymptotically approaching 1166 ± 1 cm^{-1} with a time constant of 0.66 ± 0.11 ps (Figure 8c). This time constant matches the picosecond carrier cooling timescale and suggests that the spin-orbit splitting is weakly dependent on the carrier temperature. Moreover, it is noteworthy that the asymptotic value of 1166 ± 1 cm^{-1} provides a measure of the K_{v1}–K_{v2} spin-orbit splitting of five-layer MoS_2.

Conclusion

Femtosecond optical pump-probe spectroscopy has been employed to unravel, for the first time, the separate electron and hole relaxation dynamics following photoexcitation of five-layer MoS_2, as well as the nature of phonons that participate in intra- and intervalley carrier-phonon scattering. Analysis of the first and zeroth spectral moments computed from the normalized differential transmission spectra yields timescales for intravalley and intervalley relaxation, respectively. Intravalley relaxation of the electron at K_c exhibits nonexponential decay kinetics. The Gaussian decay constant decreases from 1.77 ± 0.08 ps to 1.34 ± 0.02 ps with increasing pump fluence, suggesting the dominant role played by acoustic phonons in mediating the intravalley relaxation. With increasing pump fluence, intervalley scattering timescales are found to increase from 0.51 ± 0.01 ps to 0.67 ± 0.01 ps for scattering in the conduction band, and decrease from 1.21 ± 0.03 ps to 0.62 ± 0.01 ps for scattering in the valence band. The observed fluence dependence points to the participation of LO phonons and acoustic phonons in intervalley scattering in the conduction and valence bands, respectively. In support of this result, the second-order Raman scattering sidebands that emerge in the $\Delta T/T$ spectra under high-fluence excitation conditions suggests carrier-phonon scattering in the conduction and valence bands that involve the E_{1g} LO phonon and the LA phonon, respectively. The experimentally determined timescale for intervalley electronic relaxation are substantiated by *ab initio* nonadiabatic molecular dynamics simulations. Finally, close examination of the $\Delta T/T$ spectra reveals a two-electron radiative shake-up satellite that arises from radiative band edge carrier recombination and the concomitant excitation of holes from K_{v1} to K_{v2}. The observed two-electron transition points to the high degree of electron correlation that exists in photoexcited few-layer MoS_2.

16

Experimental and Theoretical Methods

The preparation of the five-layer MoS_2 sample by chemical vapor deposition (CVD) and its extensive characterization by various spectroscopic, microscopic, and electrical methods have been detailed previously.[66] The use of a chlorine-based precursor ($MoCl_5$) in the growth of the five-layer MoS_2 sample favors the creation of the 3R polytype.[67] Whereas the more commonly studied 2H polytype has a centrosymmetric structure, the 3R polytype is non-centrosymmetric. The different symmetry properties, however, do not significantly impact the band structure of the few-layer samples.[67] Characterization of the MoS_2 sample by atomic force and Raman microscopies reveals a spatially homogeneous, five-layer sample.[29] Optical pump-probe spectroscopy is performed with narrowband pump pulses centered at 684 nm and broadband probe pulses that span the exciton A and B transitions. The broadband probe pulses of 10-fs duration are centered at 660 nm with a spectral bandwidth of ~200 nm. The narrowband pump pulse is generated by inserting a 10-nm bandpass filter into the original broadband pump pulse. A second-order intensity cross-correlation between pump and probe pulses, performed in a 10-μm-thick BBO crystal located at the position of the sample target, reveals a time resolution of 83 fs FWHM for the apparatus (Supporting Information Figure S4). Typical pulse energies for pump and probe beams are 100 nJ and 20 nJ, respectively. The focal spot diameter ($1/e^2$) of the pump beam (400 μm) is twice that of the probe beam (200 μm). The pump and probe beams are orthogonally polarized to minimize the contribution of coherent artifacts to the measured signal, which can be further suppressed by singular-value decomposition of the two-dimensional probe wavelength-time delay dataset.[68] The transmitted probe beam is spectrally dispersed in a 300-mm spectrograph and detected on a 1024-element linear array detector. The detector has a read-out rate of 1 kHz and is synchronized to the 500-Hz optical chopper positioned in the path of the

pump beam. The differential transmission signal exhibits a linear fluence dependence in the

range of pump fluences used in the experiments (Supporting Information Figure S5). All

measurements are performed at 300 K. To minimize sample degradation by potential

atmospheric oxidation, the MoS_2 sample is housed in a vacuum cryostat that is evacuated to

$<10^{-6}$ mbar.

We applied *ab initio* nonadiabatic molecular dynamics (NAMD) implemented within

time-domain density functional theory (TD-DFT)[69–71] in the Kohn-Sham (KS) framework[72] to

model the inter- and intravalley electron-phonon relation in the K valley in a bilayer MoS_2. The

simulations were performed using the Vienna *ab initio* simulation package (VASP)[73,74]

augmented with the NAMD functionality.[75–77] The generalized gradient approximation (GGA)

functional of Perdew-Burke-Ernzerhof (PBE)[78] was used to describe the electronic exchange-

correlation interactions, while the projector augmented wave (PAW)[79] method was employed to

represent the electron-ion interaction. 15 Å of vacuum was added perpendicular to the bilayer to

avoid spurious interactions between the periodic images. The optimized bilayer MoS_2 was heated

to 300 K by repeated velocity rescaling. A microcanonical molecular dynamics trajectory of 4 ps

was run in the ground state with a 1-fs time step. The DFT-D2 method of Grimme[80] was used to

describe the van der Waals interactions stabilizing the bilayer MoS_2 during geometry

optimization and molecular dynamics simulation.

To model the photo-induced inter- and intravalley electron-phonon scattering dynamics

within the experimental excess energy range, we utilized the classical path approximation[76]

combined with the fewest switches surface hopping (FSSH)[81] into the time-domain KS scheme[72]

and including a semiclassical correction for quantum decoherence.[82] The decoherence times were

computed using the optical-response formalism, as described in ref. 83 The approach has been

applied to study electron transfer and relaxation in many systems, including graphane,[84] carbon nanoribbons,[85] and quantum dot-TiO_2 interfaces.[86] FSSH is a NAMD method using a stochastic algorithm that generates trajectory branching[81] and satisfies detailed balance.[87]

In the experiment, the electron-phonon scattering processes start with 620 cm^{-1} (~0.08 eV) of excess electron energy. To capture the dynamics within this energy range, we had to include multiple k-points. Among the 600 k-points, there were 36 k-points within the K valley. 10 k-points outside the K valley were used to describe the intervalley electron-phonon relaxation.

Supporting Information Available: Fit parameters for intravalley electronic relaxation, calculation of the excess energies of the carriers, reconstructed transmission spectrum of the photoexcited MoS_2 sample, sample characterization by resonant Raman spectroscopy, optical pump-probe cross-correlation, and fluence-dependence measurement results. This material is available free of charge *via* the Internet at http://pubs.acs.org.

References

1. Wang, Q. H.; Kalantar-Zadeh, K.; Kis, A.; Coleman, J. N.; Strano, M. S. Electronics and Optoelectronics of Two-Dimensional Transition Metal Dichalcogenides. *Nat. Nanotechnol*. **2012**, *7*, 699–712.

2. Chhowalla, M.; Shin, H. S.; Eda, G.; Li, L.-J.; Loh, K. P.; Zhang, H. The Chemistry of Two-Dimensional Layered Transition Metal Dichalcogenide Nanosheets. *Nat. Chem*. **2013**, *5*, 263–275.

3. Ganatra, R.; Zhang, Q. Few-Layer MoS_2: A Promising Layered Semiconductor. *ACS Nano* **2014**, *8*, 4074–4099.

4. Radisavljevic, B.; Radenovic, A.; Brivio, J.; Giacometti, V.; Kis, A. Single-Layer MoS_2 Transistors. *Nat. Nanotechnol*. **2011**, *6*, 147–150.

5. Splendiani, A.; Sun, L.; Zhang, Y.; Li, T.; Kim, J.; Chim, C.-Y.; Galli, G.; Wang, F. Emerging Photoluminescence in Monolayer MoS_2. *Nano Lett*. **2010**, *10*, 1271–1275.

6. Mak, K. F.; Lee, C.; Hone, J.; Shan, J.; Heinz, T. F. Atomically Thin MoS_2: A New Direct-Gap Semiconductor. *Phys. Rev. Lett*. **2010**, *105*, 136805.

7. Tongay, S.; Zhou, J.; Ataca, C.; Lo, K.; Matthews, T. S.; Li, J.; Grossman, J. C.; Wu, J. Thermally Driven Crossover from Indirect Toward Direct Bandgap in 2D Semiconductors: $MoSe_2$ versus MoS_2. *Nano Lett*. **2012**, *12*, 5576–5580.

8. Ruppert, C.; Aslan, O. B.; Heinz, T. F. Optical Properties and Band Gap of Single- and Few-Layer $MoTe_2$ Crystals. *Nano Lett*. **2014**, *14*, 6231–6236.

9. Jariwala, D.; Sangwan, V. K.; Lauhon, L. J.; Marks, T. J.; Hersam, M. C. Emerging Device Applications for Semiconducting Two-Dimensional Transition Metal Dichalcogenides. *ACS Nano* **2014**, *8*, 1102–1120.

10. Xiao, D.; Liu, G.-B.; Feng, W.; Xu, X.; Yao, W. Coupled Spin and Valley Physics in Monolayers of MoS_2 and Other Group-VI Dichalcogenides. *Phys. Rev. Lett*. **2012**, *108*, 196802.

11. Cao, T.; Wang, G.; Han, W.; Ye, H.; Zhu, C.; Shi, J.; Niu, Q.; Tan, P.; Wang, E.; Liu, B.; Feng, J. Valley-Selective Circular Dichroism of Monolayer Molybdenum Disulphide. *Nat. Commun*. **2012**, *3*, 887.

12. Zeng, H.; Dai, J.; Yao, W.; Xiao, D.; Cui, X. Valley Polarization in MoS_2 Monolayers by Optical Pumping. *Nat. Mater*. **2012**, *7*, 490–493.

13. Mak, K. F.; He, K.; Shan, J.; Heinz, T. F. Control of Valley Polarization in Monolayer MoS_2 by Optical Helicity. *Nat. Mater*. **2012**, *7*, 494–498.

14. Rycerz, A.; Tworzydło, J.; Beenakker, C. W. J. Valley Filter and Valley Valve in Graphene. *Nat. Phys*. **2007**, *3*, 172–175.

15. Das, S.; Chen, H.-Y.; Penumatcha, A. V.; Appenzeller, J. High Performance Multilayer MoS_2 Transistors with Scandium Contacts. *Nano Lett*. **2013**, *13*, 100–105.

16. Wang, H.; Yu, L.; Lee, Y.-H.; Shi, Y.; Hsu, A.; Chin, M. L.; Li, L.-J.; Dubey, M.; Kong, J.; Palacios, T. Integrated Circuits Based on Bilayer MoS_2 Transistors. *Nano Lett*. **2012**, *12*, 4674–4680.

17. Perea-López, N.; Elías, A. L.; Berkdemir, A.; Castro-Beltran, A.; Gutiérrez, H. R.; Feng, S.; Lv, R.; Hayashi, T.; López-Urías, F.; Ghosh, S.; *et al.* Photosensor Device Based on Few-Layered WS_2 Films. *Adv. Funct. Mater*. **2013**, *23*, 5511–5517.

18. Rumyantsev, S. L; Jiang, C.; Samnakay, R.; Shur, M. S.; Balandin, A. A. 1/f Noise Characteristics of MoS_2 Thin-Film Transistors: Comparison of Single and Multilayer Structures. *IEEE Electr. Device Lett*. **2015**, DOI 10.1109/LED.2015.2412536.

19. Li, H.; Yin, Z.; He, Q.; Li, H.; Huang, X.; Lu, G.; Fam, D. W. H.; Tok, A. I. Y.; Zhang, Q.; Zhang, H. Fabrication of Single- and Multilayer MoS_2 Film-Based Field-Effect Transistors for Sensing NO at Room Temperature. *Small* **2012**, *8*, 63–67.

20. Choi, W.; Cho, M. Y.; Konar, A.; Lee, J. H.; Cha, G.-B.; Hong, S. C.; Kim, S.; Kim, J.; Jena, D.; Joo, J.; Kim, S. High-Detectivity Multilayer MoS_2 Phototransistors with Spectral Response from Ultraviolet to Infrared. *Adv. Mater*. **2012**, *24*, 5832–5836.

21. Yin, Z.; Li, H.; Li, H.; Jiang, L.; Shu, Y.; Sun, Y.; Lu, G.; Zhang, Q.; Chen, X.; Zhang, H. Single-Layer MoS_2 Phototransistors. *ACS Nano* **2012**, *6*, 74–80.

22. Lee, H. S.; Min, S.-W.; Chang, Y.-G.; Park, M. K.; Nam, T.; Kim, H.; Kim, J. H.; Ryu, S.; Im, S. MoS_2 Nanosheet Phototransistors with Thickness-Modulated Optical Energy Gap. *Nano Lett*. **2012**, *12*, 3695–3700.

23. Shah, J. *Ultrafast Spectroscopy of Semiconductors and Semiconductor Nanostructures*, 2nd Edition; Springer Series in Solid-State Sciences; Springer: Berlin, 1999.

24. Wang, Q.; Ge, S.; Li, X.; Qiu, J.; Ji, Y.; Feng, J.; Sun, D. Valley Carrier Dynamics in Monolayer Molybdenum Disulfide from Helicity-Resolved Ultrafast Pump-Probe Spectroscopy. *ACS Nano* **2013**, *7*, 11087–11093.

25. Mai, C.; Barrette, A.; Yu, Y.; Semenov, Y. G.; Kim, K. W.; Cao, L.; Gundogdu, K. Many-Body Effects in Valleytronics: Direct Measurement of Valley Lifetimes in Single-Layer MoS$_2$. *Nano Lett*. **2014**, *14*, 202–206.

26. Korn, T.; Heydrich, S.; Hirmer, M.; Schmutzler, J.; Schüller, C. Low-Temperature Photocarrier Dynamics in Monolayer MoS$_2$. *Appl. Phys. Lett*. **2011**, *99*, 102109.

27. Lagarde, D.; Bouet, L.; Marie, X.; Zhu, C. R.; Liu, B. L.; Amand, T.; Tan, P. H.; Urbaszek, B. Carrier and Polarization Dynamics in Monolayer MoS$_2$. *Phys. Rev. Lett*. **2014**, *112*, 047401.

28. Sim, S.; Park, J.; Song, J.-G.; In, C.; Lee, Y.-S.; Kim, H.; Choi, H. Exciton Dynamics in Atomically Thin MoS$_2$: Interexcitonic Interaction and Broadening Kinetics. *Phys. Rev. B* **2013**, *88*, 075434.

29. Nie, Z.; Long, R.; Sun, L.; Huang, C.-C.; Zhang, J.; Xiong, Q.; Hewak, D. W.; Shen, Z.; Prezhdo, O. V.; Loh, Z.-H. Ultrafast Carrier Thermalization and Cooling Dynamics in Few-Layer MoS$_2$. *ACS Nano* **2014**, *8*, 10931–10940.

30. Sun, D.; Rao, Y.; Reider, G. A.; Chen, G.; You, Y.; Brézin, L.; Harutyunyan, A. R.; Heinz, T. F. Observation of Rapid Exciton-Exciton Annihilation in Monolayer Molybdenum Disulfide. *Nano Lett*. **2014**, *14*, 5625–5629.

31. Hong, X.; Kim, J.; Shu, S.-F.; Zhang, Y.; Jin, C.; Sun, Y.; Tongay, S.; Wu, J.; Zhang, Y.; Wang, F. Ultrafast Charge Transfer in Atomically Thin MoS$_2$/WS$_2$ Heterostructures. *Nat. Nanotechnol*. **2014**, *9*, 682–686.

32. Wang, R.; Ruzicka, B. A.; Kumar, N.; Bellus, M. Z.; Chiu, H.-Y.; Zhao, H. Ultrafast and Spatially Resolved Studies of Charge Carrier in Atomically Thin Molybdenum Disulfide. *Phys. Rev. B* **2012**, *86*, 045406.

33. Shi, H.; Yan, R.; Bertolazzi, S.; Brivio, J.; Gao, B.; Kis, A.; Jena, D.; Xing, H. G.; Huang, L. Exciton Dynamics in Suspended Monolayer and Few-Layer MoS_2 2D Crystals. *ACS Nano* **2013**, *7*, 1072–1080.

34. Lui, C. H.; Frenzel, A. J.; Pilon, D. V.; Lee, Y.-H.; Ling, X.; Akselrod, G. M.; Kong, J.; Gedik, N. Trion-Induced Negative Photoconductivity in Monolayer MoS_2. *Phys. Rev. Lett.* **2014**, *113*, 166801.

35. Docherty, C. J.; Parkinson, P.; Joyce, H. J.; Chiu, M.-H.; Chen, C.-H.; Lee, M.-Y.; Li, L.-J.; Herz, L. M.; Johnston, M. B. Ultrafast Transient Terahertz Conductivity of Monolayer MoS_2 and WSe_2 Grown by Chemical Vapor Deposition. *ACS Nano* **2014**, *8*, 11147–11153.

36. Oudar, J. L.; Hulin, D.; Migus, A.; Antonetti, A.; Alexandre, F. Subpicosecond Spectral Hole Burning Due to Nonthermalized Photoexcited Carriers in GaAs. *Phys. Rev. Lett.* **1985**, *55*, 2074–2077.

37. Alexandrou, A.; Berger, V.; Hulin, D. Direct Observation of Electron Relaxation in Intrinsic GaAs Using Femtosecond Pump-Probe Spectroscopy. *Phys. Rev. B* **1995**, *52*, 4654–4657.

38. Camescasse, F. X.; Alexandrou, A.; Hulin, D.; Bányai, L.; Tran Thoai, D. B.; Haug, H. Ultrafast Electron Redistribution through Coulomb Scattering in Undoped GaAs: Experiment and Theory. *Phys. Rev. Lett.* **1996**, *77*, 5429–5432.

39. Radisavljevic, B.; Kis, A. Mobility Engineering and a Metal-Insulator Transition in Monolayer MoS_2. *Nat. Mater.* **2013**, *12*, 815–820.

40. *Gmelin Handbook of Inorganic and Organometallic Chemistry*, 8th Edition; Springer-Verlag: Berlin, 1995; Vol. B7.

41. Kuc, A.; Zibouche, N.; Heine, T. Influence of Quantum Confinement on the Electronic Structure of the Transition Metal Sulfide TS$_2$. *Phys. Rev. B* **2011**, *83*, 245213.

42. Othonos, A. Probing Ultrafast Carrier and Phonon Dynamics in Semiconductors. *J. Appl. Phys.* **1998**, *83*, 1789–1830.

43. Molina-Sánchez, A.; Sangalli, D.; Hummer, K.; Marini, A.; Wirtz, L. Effect of Spin-Orbit Interaction on the Optical Spectra of Single-Layer, Double-Layer, and Bulk MoS$_2$. *Phys. Rev. B* **2013**, *88*, 045412.

44. Kuc, A.; Zibouche, N.; Heine, T. Influence of Quantum Confinement on the Electronic Structure of the Transition Metal Sulfide *T*S$_2$. *Phys. Rev. B* **2011**, *83*, 245213.

45. Pollard, W. T.; Lee, S.-Y.; Mathies, R. A. Wave Packet Theory of Dynamic Absorption Spectra in Femtosecond Pump-Probe Experiments. *J. Chem. Phys.* **1990**, *92*, 4012–4029.

46. Shank, C. V.; Fork, R. L.; Leheny, R. F.; Shah, J. Dynamics of Photoexcited GaAs Band-Edge Absorption with Subpicosecond Resolution. *Phys. Rev. Lett.* **1979**, *42*, 112–115.

47. Erskine, D. J.; Taylor, A. J.; Tang, C. L. Dynamic Burstein-Moss Shift in GaAs and GaAs/AlGaAs Multiple Quantum Well Structures. *Appl. Phys. Lett.* **1984**, *45*, 1209–1211.

48. Kilina, S. V.; Craig, C. F.; Kilin, D. S.; Prezhdo, O. V. Ab Initio Time-Domain Study of Phonon-Assisted Relaxation of Charge Carriers in a PbSe Quantum Dot. *J. Phys. Chem. C* **2007**, *111*, 4871–4878.

49. Kilina, S. V.; Kilin, D. S.; Prezhdo, O. V. Breaking the Phonon Bottleneck in PbSe and CdSe Quantum Dots: Time-Domain Density Functional Theory of Charge Carrier Relaxation. *ACS Nano* **2009**, *3*, 93–99.

50. Kaasbjerg, K.; Thygesen, K. S.; Jacobsen, K. W. Phonon-Limited Mobility in n-Type Single-Layer MoS_2 from First Principles. *Phys. Rev. B* **2012**, *85*, 115317.

51. Li, X.; Mullen, J. T.; Jin, Z.; Borysenko, K. M.; Nardelli, M. B.; Kim, K. W. Intrinsic Electrical Transport Properties of Monolayer Silicene and MoS_2 from First Principles. *Phys. Rev. B* **2013**, *87*, 115418.

52. Kaasbjerg, K.; Bhargavi, K. S.; Kubakaddi, S. S. Hot-Electron Cooling by Acoustic and Optical Phonons in Monolayers of MoS_2 and Other Transition-Metal Dichalcogenides. *Phys. Rev. B* **2014**, *90*, 165436.

53. Shah, J.; Pinczuk, A.; Gossard, A. C.; Wiegmann, W. Energy-Loss Rates for Hot Electrons and Holes in GaAs Quantum Wells. *Phys. Rev. Lett*. **1985**, *54*, 2045–2048.

54. Breusing, M.; Kuehn, S.; Winzer, T.; Malić, E.; Milde, F.; Severin, N.; Rabe, J. P.; Ropers, C.; Knorr, A.; Elsaesser, T. Ultrafast Nonequilibrium Carrier Dynamics in a Single Graphene Layer. *Phys. Rev. B* **2011**, *83*, 153410.

55. Chen, J. M.; Wang, C. S. Second Order Raman Spectrum of MoS_2. *Solid State Commun*. **1974**, *14*, 857–860.

56. Ferrari, A. C.; Basko, D. M. Raman Spectroscopy as a Versatile Tool for Studying the Properties of Graphene. *Nat. Nanotechnol*. **2013**, *8*, 235–242.

57. Stacy, A. M.; Hodul, D. T. Raman Spectra of IVB and VIB Transition Metal Disulfides Using Laser Energies Near the Absorption Edges. J. Phys. Chem. Solids **1985**, *46*, 405–409.

58. Chakraborty, B.; Ramakrishna Matte, H. S. S.; Sood, A. K.; Rao, C. N. R. Layer-Dependent Resonant Raman Scattering of a Few Layer MoS$_2$. *J. Raman Spectrosc*. **2013**, *44*, 92–96.

59. Zeng, H.; Zhu, B.; Liu, K.; Fan, J.; Cui, X.; Zhang, Q. M. Low-Frequency Raman Modes and Electronic Excitations in Atomically Thin MoS$_2$ Films. *Phys. Rev. B* **2012**, *86*, 241301(R).

60. Gołasa, K.; Grzeszcyzk, M.; Leszczyński, P.; Faugeras, C.; Nicolet, A. A. L.; Wysmolek, A.; Potemski, M.; Babinski, A. Multiphonon Resonant Raman Scattering in MoS$_2$. *Appl. Phys. Lett*. **2014**, *104*, 092106.

61. Bloch, F. Double Electron Transitions in X-Ray Spectra. *Phys. Rev*. **1935**, *48*, 187–192.

62. Wang, X.; Ren, X.; Kahen, K.; Hahn, M. A.; Rajeswaran, M.; Maccagnano-Zacher, S.; Silcox, J.; Cragg, G. E.; Efros, A. L.; Krauss, T. D. Non-Blinking Semiconductor Nanocrystals. *Nature* **2009**, *459*, 686–689.

63. Dean, P. J.; Cuthbert, J. D.; Thomas, D. G.; Lynch, R. T. Two-Electron Transitions in the Luminescence of Excitons Bound to Neutral Donors in Gallium Phosphide. *Phys. Rev. Lett*. **1967**, *18*, 122–124.

64. Dean, P. J.; Haynes, J. R.; Flood, W. F. New Radiative Recombination Processes Involving Neutral Donors and Acceptors in Silicon and Germanium. *Phys. Rev*. **1967**, *161*, 711–729.

65. Tanner, G.; Richter, K.; Rost, J.-M. The Theory of Two-Electron Atoms: Between Ground State and Complete Fragmentation. *Rev. Mod. Phys*. **2000**, *72*, 497–544.

66. Huang, C.-C.; Al-Saab, F.; Wang, Y.; Qu, J.-Y.; Walker, J. C.; Wang, S.; Gholipour, B.; Simpson, R. E.; Hewak, D. W. Scalable High-Mobility MoS$_2$ Thin Films Fabricated by an

Atmospheric Pressure Chemical Vapor Deposition Process at Ambient Temperature. *Nanoscale* **2014**, *6*, 12792–12797.

67. Suzuki, R.; Sakano, M.; Zhang, Y. J.; Akashi, R.; Morikawa, D.; Harasawa, A.; Yaji, K.; Kuroda, K.; Miyamoto, K.; Okuda, T.; et al. Valley-Dependent Spin Polarization in Bulk MoS_2 with Broken Inversion Symmetry. *Nat. Nanotech*. **2014**, *9*, 611–617.

68. Dobryakov, A. L.; Kovalenko, S. A.; Ernsting, N. P. Electronic and Vibrational Coherence Effects in Broadband Transient Absorption Spectroscopy with Chirped Supercontinuum Probing. *J. Chem. Phys*. **2003**, *119*, 988–1002.

69. Gross, E. K. U.; Kohn, W. Local Density-Functional Theory of Frequency-Dependent Linear Response. *Phys. Rev. Lett*. **1985**, *55*, 2850–2852.

70. Li, X.; Tully, J. C.; Schlegel, H. B.; Frisch, M. J. *Ab Initio* Ehrenfest Dynamics. *J. Chem. Phys*. **2005**, *123*, 084106.

71. Tretiak, S.; Igumenshchev, K.; Chernyak, V. Exciton Sizes of Conducting Polymers Predicted by Time-Dependent Density Functional Theory. *Phys. Rev. B* **2005**, *71*, 033201.

72. Kohn, W.; Sham, L. J. Self-Consistent Equations Including Exchange and Correlation Effects. *Phys. Rev*. **1965**, *140*, A1133–A1138.

73. Kresse, G.; Furthmüller, J. Efficient Iterative Schemes for Ab Initio Total-Energy Calculations Using a Plane-Wave Basis Set. *Phys. Rev. B* **1996**, *54*, 11169–11186.

74. Kresse, G.; Hafner, J. *Ab Initio* Molecular Dynamics for Liquid Metals. *Phys. Rev. B* **1993**, *47*, 558–561.

75. Craig, C. F.; Duncan, W. R.; Prezhdo, O. V. Trajectory Surface Hopping in the Time-Dependent Kohn-Sham Approach for Electron-Nuclear Dynamics. *Phys. Rev. Lett*. **2005**, *95*, 163001.

76. Akimov, A. V.; Prezhdo, O. V. The PYXAID Program for Non-Adiabatic Molecular Dynamics in Condensed Matter Systems. *J. Chem. Theor. Comput*. **2013**, *9*, 4959–4972.

77. Akimov, A. V.; Prezhdo, O. V. Advanced Capabilities of the PYXAID Program: Integration Schemes, Decoherence Effects, Multiexcitonic States, and Field-Matter Interaction. *J. Chem. Theor. Comput*. **2014**, *10*, 789–804.

78. Perdew, J. P.; Burke, K.; Ernzerhof, M. Generalized Gradient Approximation Made Simple. *Phys. Rev. Lett*. **1996**, *77*, 3865–3868.

79. Blöchl, P. E. Projector Augmented-Wave Method. *Phys. Rev. B* **1994**, *50*, 17953–17979.

80. Grimme, S. Semiempirical GGA-Type Density Functional Constructed with a Long-Range Dispersion Correction. *J. Comput. Chem*. **2006**, *27*, 1787–1799.

81. Tully, J. C. Molecular Dynamics with Electronic Transitions. *J. Chem. Phys*. **1990**, *93*, 1061–1071.

82. Habenicht, B. F.; Prezhdo, O. V. Nonradiative Quenching of Fluorescence in a Semiconducting Carbon Nanotube: A Time-Domain *Ab Initio* Study. *Phys. Rev. Lett*. **2008**, *100*, 197402.

83. Madrid, A. B.; Kim, H.-D.; Habenicht, B. F; Prezhdo, O. V. Phonon-Induced Dephasing of Excitons in Semiconductor Quantum Dots: Multiple Exciton Generation, Fission, and Luminescence. *ACS Nano* **2009**, *3*, 2487–2494.

84. Nelson, T. R.; Prezhdo, O. V. Extremely Long Nonradiative Relaxation of Photoexcited Graphane is Greatly Accelerated by Oxidation: Time-Domain *Ab Initio* Study. *J. Am. Chem. Soc*. **2013**, *135*, 3702–3710.

85. Habenicht, B. F.; Prezhdo, O. V. Time-Domain *Ab Initio* Study of Nonradiative Decay in a Narrow Graphene Ribbon. *J. Phys. Chem. C* **2009**, *113*, 14067–14070.

86. Long. R.; English, N. J.; Prezhdo, O. V. Minimizing Electron-Hole Recombination on TiO_2 Sensitized with PbSe Quantum Dots: Time-Domain *Ab Initio* Analysis. *J. Phys. Chem. Lett*. **2014**, *5*, 2941–2946.

87. Parandekar, P. V.; Tully, J. C. Mixed Quantum-Classical Equilibrium *J. Chem. Phys*. **2005**, *122*, 094102.

Table 1. Time constants for intervalley scattering of electrons and holes from the K valley as a function of carrier density, extracted from the decays of $\langle \lambda_B^{(0)}(t) \rangle$ and $\langle \lambda_{A-B}^{(0)}(t) \rangle$, respectively.

Fluence (mJ/cm^2)	Carrier density (10^{13} cm^{-2})	$\tau_e^{(0)}$ (ps)	$\tau_h^{(0)}$ (ps)
0.06	0.5	0.51 ± 0.01	1.21 ± 0.03
0.14	1.2	0.62 ± 0.01	0.80 ± 0.01
0.29	2.4	0.67 ± 0.01	0.62 ± 0.01
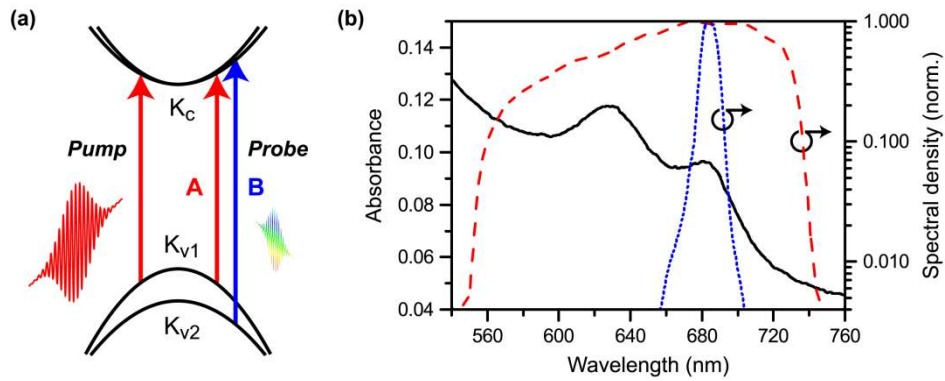
Figure 1. (a) Schematic illustration for the band-selective probing of ultrafast electron and hole relaxation dynamics in MoS_2. Following resonant excitation of the exciton A transition, the exciton B probe interrogates only the electron dynamics at K_c. With knowledge of the electron dynamics, the hole dynamics at K_{v1} can be extracted from the exciton A probe signal, which reflects both electron and hole dynamics. (b) UV/visible absorption spectrum of the five-layer MoS_2 sample collected at 300 K (solid line). The A and B excitonic transitions are located at 684 nm and 631 nm, respectively. The normalized spectral densities of the narrowband (dotted line) and broadband (dashed line) laser pulses employed for pump and probe, respectively, are also shown.
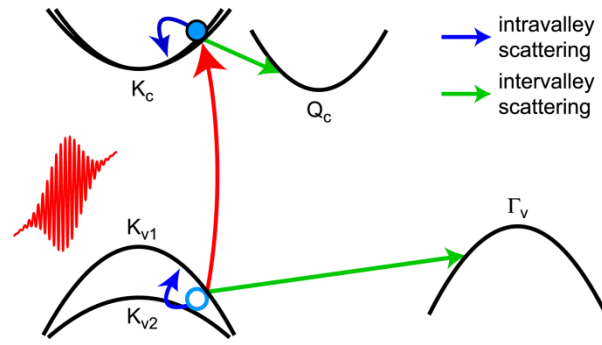
Figure 2. Schematic illustration of the various phonon-mediated carrier relaxation pathways following the photoexcitation of few-layer MoS_2 at the exciton A transition. Intravalley relaxation (blue arrows) confines the carriers to the K valley, whereas intervalley scattering (green arrows) results in the transfer of electrons and holes to the Q and Γ valleys, respectively. Carrier cooling *via* intravalley relaxation modifies the valence-to-conduction band transition energy, which in turn leads to a shift in the spectral first moment with time. On the other hand, intervalley scattering removes carriers from the K valley probe region, thereby resulting in a decrease in the spectral zeroth moment with time.
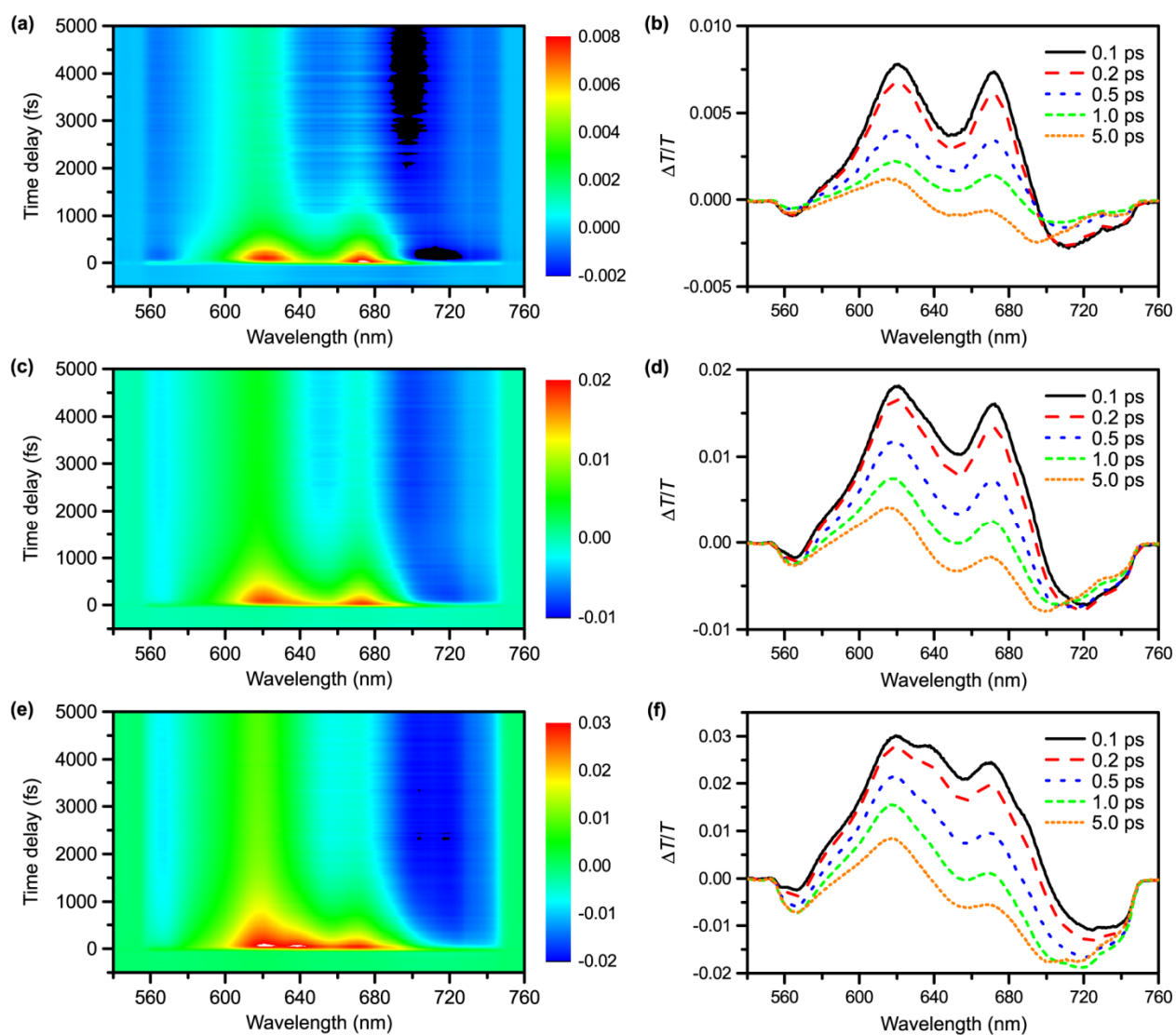
Figure 3. Normalized differential transmission $\Delta T/T$ spectra collected as a function of time delay following photoexcitation of five-layer MoS_2 with pump fluences of (a),(b) 0.06 mJ/cm^2, (c),(d) 0.14 mJ/cm^2, and (e),(f) 0.29 mJ/cm^2.
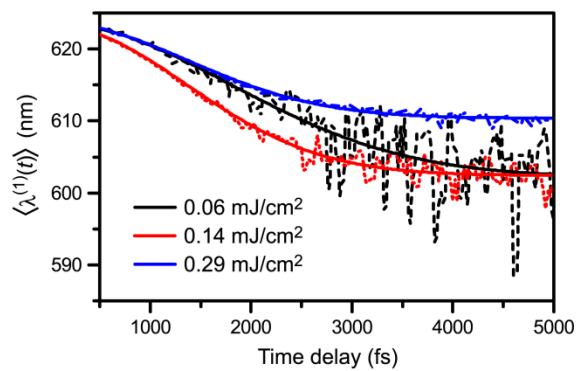
Figure 4. Time-evolution of the spectral first moment $\langle \lambda^{(1)}(t) \rangle$ computed at the exciton B probe transition (dashed lines). The spectral blueshift with time delay, which reflects intravalley relaxation of the electrons, can be adequately fit to a Gaussian function (solid lines).
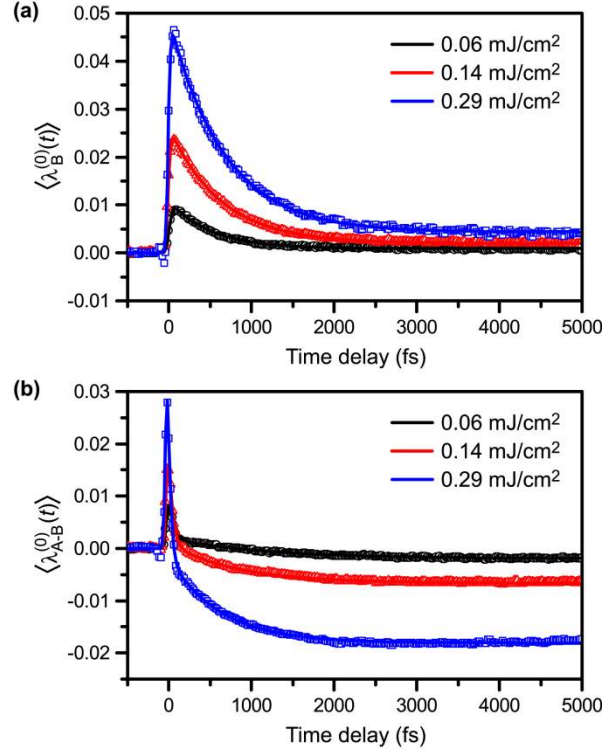
Figure 5. (a) Zeroth moment $\langle \lambda_B^{(0)}(t) \rangle$ time traces obtained at different excitation fluences. The solid lines are obtained from fitting the data to the convolution of a monoexponential decay function with a Gaussian function of 83-fs FWHM. The latter models the instrument response function. The monoexponential decay constant corresponds to $\tau_e^{(0)}$, the intervalley scattering time constant for electrons. (b) Zeroth moment $\langle \lambda_{A-B}^{(0)}(t) \rangle$ time traces obtained at different excitation fluences. The solid lines are obtained from fitting the data to the convolution of a biexponential decay function with a Gaussian function of 83-fs FWHM. The latter models the instrument response function. The slow decay component, with a time constant $\tau_h^{(0)}$, results from the intervalley scattering of holes. The origin of the fast decay component ($\tau \sim 40$ fs) is unknown, although its time constant is reminiscent of the time scale for carrier thermalization.
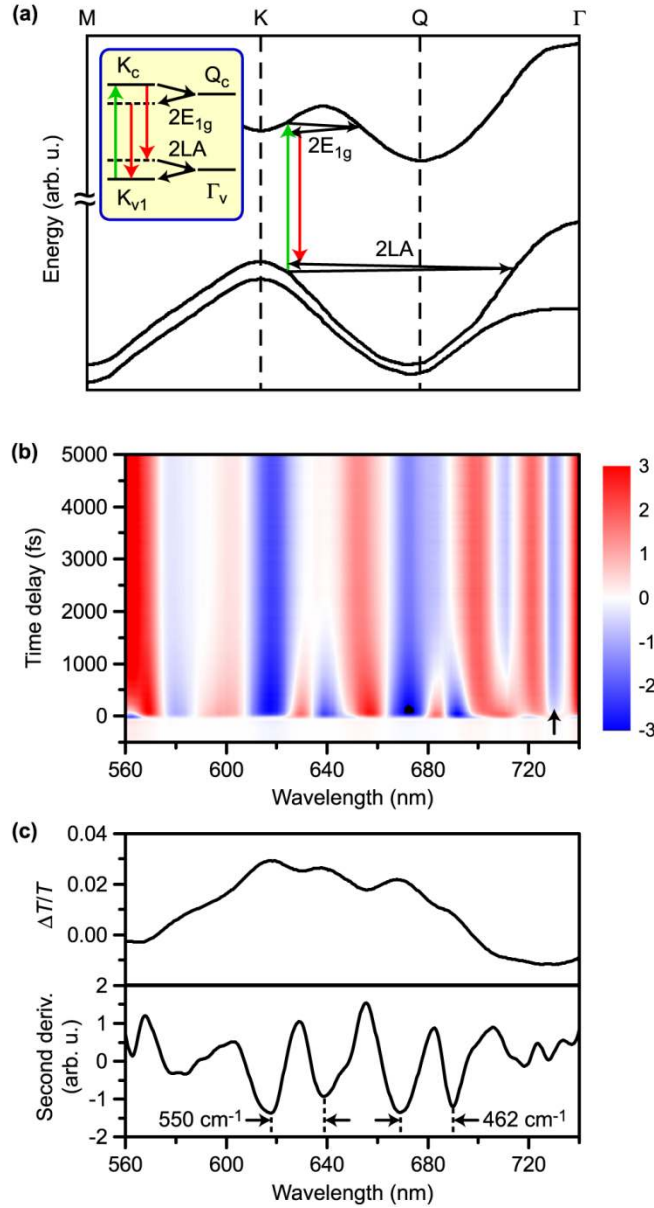
Figure 6. (a) Schematic illustration of two-phonon scattering in the conduction and valence

bands of five-layer MoS$_2$, mediated by the E$_{1g}$ LO and LA phonons, respectively. These

scattering pathways result in the appearance of second-order Raman sidebands in the $\Delta T/T$

spectra. The inset shows the energy levels that are involved in the second-order Raman

transitions. The dashed lines denote final states that are accessed by two-phonon carrier-phonon

scattering, from which the Raman sidebands originate. (b) Second-derivative spectra as a

function of time delay, obtained with an excitation fluence of 0.29 mJ/cm^2. Peaks in the $\Delta T/T$ spectra correspond to negative minima in the second-derivative spectra. The arrow denotes the position of the two-electron shake-up satellite. (c) $\Delta T/T$ spectrum (top panel) and its corresponding second-derivative spectrum (bottom panel) collected at 200-fs time delay and 0.29-mJ/cm^2 excitation fluence. Energy splittings of 462 and 550 cm^{-1} are observed at the exciton A and B transitions, respectively.
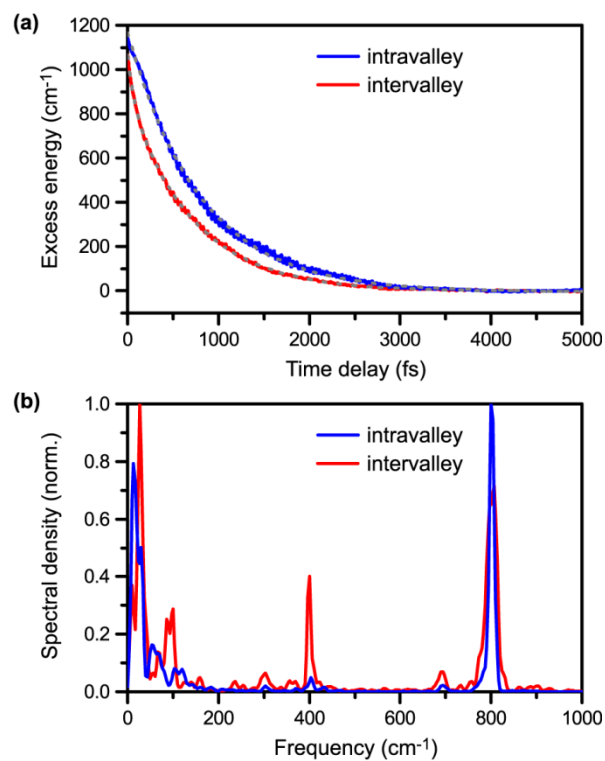
Figure 7. (a) Time traces of intravalley and intervalley electronic relaxation dynamics in the conduction band, as obtained from *ab initio* nonadiabatic molecular dynamics simulations. The dotted lines are exponential fits. (b) FFT power spectra of the electronic relaxation dynamics, revealing the frequencies of phonons that mediate the intravalley and intervalley relaxation processes.
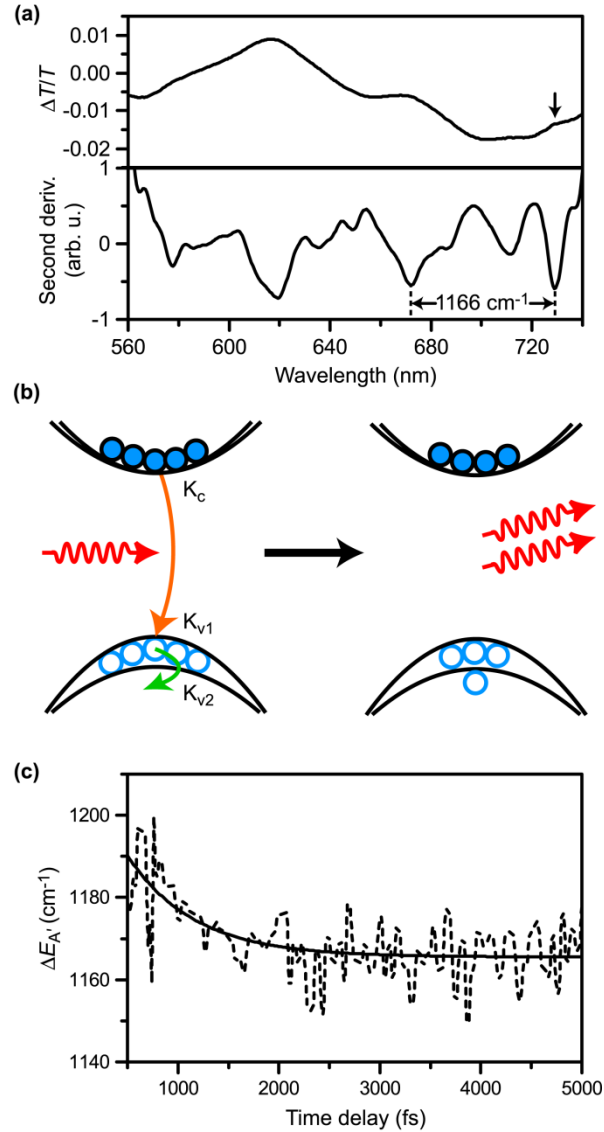
Figure 8. (a) $\Delta T/T$ spectrum (top panel) and its corresponding second-derivative spectrum (bottom panel) collected at 5-ps time delay and 0.29-mJ/cm^2 excitation fluence. A peak (dip) in the $\Delta T/T$ spectrum (second-derivative spectrum), denoted by an arrow, is observed at 729 nm. This spectral feature is redshifted by 1166 cm^{-1} relative to the exciton A transition. (b) Schematic illustration of the two-electron radiative shake-up process, in which the probe pulse stimulates radiative carrier recombination that is accompanied by the excitation of a hole from K_{v1} to K_{v2}. The amount of redshift $\Delta E_{A'}$ of the resultant two-electron satellite relative to the exciton A

transition corresponds to the spin-orbit splitting. (c) Time-evolution of $\Delta E_{A'}$ (dashed line)

converging to a value of 1166 ± 1 cm^{-1} with a time constant of 0.66 ± 0.11 ps (solid line fit).

TOC Graphic